HHS Public Access

Author manuscript

Magn Reson Imaging Clin N Am. Author manuscript; available in PMC 2022 February 01.

Published in final edited form as:

Magn Reson Imaging Clin N Am. 2021 February ; 29(1): e1–e19. doi:10.1016/j.mric.2020.10.001.

Progress in Imaging the Human Torso at the Ultrahigh Fields of 7 and 10.5 T

Kamil Uğurbil*, **Pierre-Francois Van de Moortele**, **Andrea Grant**, **Edward J. Auerbach**, **Arcan Ertürk**, **Russell Lagore**, **Xiaoxuan He**, **Gregor Adriany**, **Gregory J. Metzger**

Center for Magnetic Resonance Research (CMRR), University of Minnesota, Minneapolis, MN 55416, USA

Keywords

Torso; Ultrahigh fields; 7 T; 10.5 T; Imaging

INTRODUCTION

The provenance of the recent but exploding interest in ultrahigh magnetic fields (UHF, defined as 7 T (T) and higher) can be traced back to efforts initiated in the mid-70s aimed at extracting biological information from intact biological systems nondestructively using magnetic resonance spectroscopy and, in particular, to the development of functional MR imaging (fMR imaging) to map neuronal activity in the brain.[1] These efforts introduced disruptive new technologies and catalyzed the pursuit of new magnetic resonance (MR) instrumentation, including the development of UHF. Motivated by the promise of high magnetic fields to accelerate discoveries in brain science, several preclinical and human UHF MR imaging systems were designed and constructed including the first whole-body 7 T system installed in 1999 at the Center for Magnetic Resonance Research (CMRR) at the University of Minnesota.[1,2] This passively shielded scanner inspired subsequent commercial efforts. Although functional mapping in the human brain was initially the primary mission for this scanner, soon after the focus was extended to imaging in the human torso,[3] a much more challenging target for UHF ambitions. From this point forward, the increased availability of commercial 7 T systems from major manufacturers and the technologies introduced to solve the problems encountered in the brain at 7 T[1,4] ultimately led to the successful expansion of the UHF applications to the entire human body in order to exploit unique advantages that UHF provides (eg, reviews,[5–12]); in this article, the authors review some of the distinct UHF challenges that had to be met to accomplish this goal. These topics were also covered in part in other reviews by us with different emphasis and overall content[1,4]; these reviews may also be of interest to the reader. The 10.5 T data presented were published recently in a paper.[13]

*Corresponding author. ugurb001@umn.edu.

RADIOFREQUENCY INTERACTIONS IN THE HUMAN BODY AT 7 T

The most frequently cited advantage of UHF,[12] which justifies both further developing the technology and establishing its safety for human investigations, is the increase in signal-to-noise ratio (SNR). Electromagnetic (EM) simulations suggest that the ultimate intrinsic SNR[14,15] in MR measurements increases with the magnetic field strength, displaying supralinear gains in objects mimicking the human body, depending on the magnetic field strength and spatial location.[16,17] Field-dependent supralinear SNR gains have also been reported in experimental measurements.[18–20] Although experimentally realizable SNR must also account for specifics of the instrumentation used and acquisition and anatomy specific relaxation effects, this underlying increase in ultimate intrinsic SNR plays an important role in the overall benefits expected from high magnetic fields. Other significant UHF advantages include improved parallel imaging performance,[21] increased susceptibility-based contrast for improved anatomic and functional imaging,[22] increased chemical shift dispersion for improved spectroscopic quantification,[23,24] shifting exchange to faster regimes for improved chemical exchange saturation transfer studies,[25] and increased longitudinal relaxation times for improved noncontrast-enhanced arterial spin labeling of perfusion, in-flow angiography, [11,26,27] and 4-dimensional flow acquisitions.[28,29]

In order to realize these benefits, nontrivial challenges had to be overcome with the most significant being the transmit B_1 (B_1^+) field heterogeneities, which scale in complexity with the size of the imaging region of interest (ROI). As the RF wavelength used in MR becomes shorter than the dimensions of the object to be imaged, significant B_1^+ distortions occur, which depend on tissue EM properties and object size and geometry.[30,31] Deleterious consequences of such complex B_1 behavior at high magnetic fields was prominently visible in early efforts that aimed at increasing the operational magnetic fields to 4 T at a time when high-end clinical MR imaging scanners operated at 1.5 T. Initial results[32,33] at 4 T revealed that at such a high magnetic field, imaging the human body faced new challenges associated with dramatic image inhomogeneities both in the human head and torso. Originally, these homogeneity issues were described as resulting from “dielectric resonances.” Ultimately, however, the RF phenomenon was better characterized as an attenuated traveling wave based on early 7 T experiments examining the physics of RF behavior at ~300 MHz (proton resonance frequency at 7 T) in the conductive tissues of the human body.[34]

Fig. 1 illustrates calculations from Yang and colleagues[34] showing 2-dimensional plots of instantaneous transverse $|B_1|$ at progressive time points in phantoms with different conductivities generated by placing a surface coil on one side of the phantom. The cross-section of the RF coil is visible as 2 small bright circles to the left of the phantom, especially in the left-most column. The line drawings display signal intensity traces along a line that cuts through the middle of the phantom and the coil. At zero conductivity, a one-wavelength standing wave (ie, a “resonance”) is established (leftmost column, see Fig. 1); under this condition, excitation is simply not possible in certain areas, such as the middle of this standing wave. At higher conductivities approximating human tissue (rightmost column, see Fig. 1), the RF wave is attenuated and a more familiar surface coil profile emerges. These calculations were experimentally verified at 7 T.[34] Thus the image signal intensity can become highly nonuniform as the result of the spatial phase distribution and amplitude

modulation by the interference of the RF traveling waves determined by a given sample-coil configuration.[34]

In an object similar to the approximately spherically symmetric human head, where azimuthally distributed elements in an RF coil are used to generate a transmit B_1 field, this attenuated traveling wave behavior leads to what can be a complex interaction of the waves emanating from each of the current carrying elements. When driven in a circularly polarized mode, where each element has a transmit phase equivalent to its azimuthal position, the RF waves constructively interfere in the center of the brain, whereas in the periphery they largely interact destructively,[35] leading to the well-known center bright B_1 fields (Fig. 2). The B_1^+ is highly nonuniform within each of the transverse slices shown and the extent of this nonuniformity and B_1 magnitude changes in the head-foot direction (ie, z-direction) as well. Such nonuniformities have been the cause of center bright human head images,[19] especially if 180° pulses were involved. However, it should be recognized that many sequences also produce relatively flat images despite the presence of B_1^+ inhomogeneities because they have some intrinsic insensitivity to the flip angle (FA). Modified driven equilibrium Fourier transform (MDEFT) and rapidly acquired Gradient recalled echo (GRE) images are an example of this. In MDEFT, RF pulses used have nominally 90° and 180° FA; however, the FA achieved deviates from these nominal values due to B_1^+ inhomogeneities; nevertheless, the intervals specified in MDEFT between the 90° and 180° pulses assure signal intensity and brain tissue contrast are not sensitive to flip angle variations.[36,37] Fast GRE acquisitions can also seem to be flat under certain conditions due to the interplay between FA and relaxation rates.

In the human torso, the problem becomes even more complex because of the large body dimensions relative to the wavelength (approximately 11 cm at 7 T). An example of this is illustrated in Fig. 3, which shows simulation of the transmit B_1 field for a circumscribing body volume coil. When unloaded, this coil generates a highly uniform B_1^+ (see Fig. 3, upper panel) within its physical boundaries; however, when the human body is inserted into the coil, the B_1^+ field propagates as a wave and even ends up strongest in the human head even though the head is very much outside the RF coil (see Fig. 3, lower panel). Understanding these complexities inherent at UHF frequencies ultimately led to the development of acquisition methods, RF hardware, and RF management strategies that allowed significant progress to be made in UHF MR imaging of the human head and the torso.

Fig. 4A shows an image of a single slice through the pelvis region of the human body obtained at 4 T in early work[33] and highlights the presence of major problems. The ability to manipulate the transmit RF is ultimately necessary to overcome the aforementioned problems that are responsible for this poor image quality. This was accomplished using multichannel transmitters with channel-specific independent control.[38–40] The multichannel approach, particularly combined with local transmit coil arrays placed in close proximity to the torso, introduced the ability to maximize and/or homogenize the B_1^+ over a predetermined ROI, enabling imaging of targeted organs in the human torso at 7 T for the first time.[27,39,41–46] Fig. 4B illustrates this, showing that the problems that resulted in the poor torso images at 4 T (see Fig. 4A) can be solved even at 7 T, yielding exquisite cardiac

anatomy, the organ targeted in this study.[41,44] Fig. 4C, D show B_1^+ maps in an axial slice as in Fig. 4B, demonstrating that B_1^+ is both inhomogeneous and weak (see Fig. 4C) over the heart using a default transmit mode.[41,44] However, with B_1^+ shimming techniques, RF uniformity and magnitude is improved over the target (see Fig. 4D), leading to 7 T images of the type illustrated in Fig. 4B.

Since the original work from our laboratory,[39,41,42] imaging in the human torso using multichannel parallel transmit (pTx) techniques and local multichannel transmit and receive array coils have been adapted and used for human torso studies by other groups as well (eg, [47–59]) and is a growing endeavor. These efforts have resulted in diverse coil geometries (eg, [39,57]). Significant further developments in this area are expected, including larger number of transmit and receive coils, advanced pulse designs such as multispoke pulses for improved B_1^+ homogeneity, and significantly higher accelerations in image acquisition through the use of the multiband technique for simultaneous slice excitation together with k-space undersampling in the phase encode direction. An interesting extension of the B_1^+ phase and magnitude shimming (ie, one spoke) approach is time interleaved acquisition of modes; this approach has been shown to significantly improve image homogeneity with minimal impact on overall acquisition time through the use of a virtual coil reconstruction.[48] Two-spoke pulses have been used with 16 channel transmitters yielding significant improvements in spatial homogeneity of contrast and signal intensity over the heart.[45] Similarly, using the principles described by Wu and colleagues,[60] slice acceleration using pTx multiband pulses to optimize B_1^+ with a power parameter regularization has been demonstrated in the heart as well.[61] Substantial new improvements in such techniques are expected in the future as implementation workflows are improved, including robust and rapid acquisition of calibration data, rapid calculation of RF shims or pTx pulses, and implementation of real-time power monitoring.

In combination with B_1^+ homogeneity issues, challenges related to limitations in peak achievable B_1^+ and concerns of local heating present further problems exacerbated by the geometry and size of the human torso.[12] Addressing these interrelated issues has involved the constant development of RF transmit chain technologies, RF management strategies, and RF coil developments, each motivating the other. In contrast to lower field systems, local rather than global power deposition and heating becomes a primary limitation as governed by the International Electrotechnical Commission guidelines.[62] Local power deposition is characterized by the specific absorption rate (SAR) given in W/kg averaged greater than 10 g and is estimated through EM simulations of specific RF coils in human body models. RF coil simulations are typically performed as part of a coil validation process, which is often negotiated between a site and their local regulatory agencies. An example of a comprehensive validation procedure has been described by Hoffmann and colleagues.[63]

Beyond RF-related issues, physiologic confounders are increasingly impactful and become more difficult to manage at UHF in body applications.[12] First, motion in the torso directly competes with the goal of exploiting SNR advantages to obtain higher resolution data. Second, the linear scaling of susceptibility effects with field strength, which is beneficial in some areas such as fMR imaging, becomes a challenging issue when considering larger scale, motion-induced, temporally varying static field inhomogeneities.[64] Third, common

strategies for triggering and gating are compromised at UHF. Field strength-dependent magnetohydrodynamic effects obscure the T wave used in standard cardiac triggering,[65] and standard navigator strategies can be hindered by the same RF inhomogeneities affecting image contrast.[28,29,66–68]

Radiofrequency Coils

The conventional approach used in clinical imagers for imaging the body is to use a large circumscribing "body" RF coil for RF transmission; this coil resides behind the bore liner that defines the patient accessible space, whereas signal reception is achieved using local coil arrays placed in close proximity to the target of interest in the human body. Although similar whole-body transmitters[3,39] with local receive arrays[69,70] were originally explored for 7 T, the ability to generate the B_1^+ necessary for many standard imaging sequences was not possible because of the limitations in the transmit chain mainly due to the limited power available from the RF amplifiers used, coupled with poor transmit efficiency of the systems. Despite these challenges, new strategies for exploring the potential of integrated whole body ^{1}H transmit RF coils continues.[71,72]

In the absence of a viable whole-body proton transmitter solution, the workhorse for most UHF body imaging applications have been close-fitting local transmit and receive (ie, transceiver) arrays.[44,56,59,73–79] The first arrays were larger scale versions of those successfully implemented for imaging the human head.[38] These transceiver arrays, developed both independently and in collaborations by several groups, illustrate the variety of attempts that have been conducted to improve transmit and/or receive performance. On the receive side, design criteria include improved sensitivity and parallel imaging performance. On the transmit side, the focus has been on decreasing peak local SAR (W/kg) and increasing transmit efficiency ($B_1^+/W^{0.5}$), SAR efficiency ($B_1^+/SAR^{0.5}$), and in combination with the RF transmit chain, peak achievable B_1^+.

Recently, several groups have begun to explore and evaluate the addition of separate receive-only elements along with the transmit side technologies for body arrays.[80,81] Minimizing interferences between receive and transmit elements, maintaining acceptable transmit performance, and developing a robust, practical, and comfortable mechanical housing are among some of the issues that need to be addressed with this approach.

We illustrate examples of RF coils used for imaging in the human torso using prostate and cardiac MR imaging as anatomic targets. The prostate was an ideal target to evaluate coil performance and explore body imaging at 7 T because of its relatively small size and central location in the pelvis. Its size and location made it possible to use the most basic RF shimming strategies {Metzger, 2008 #34} to optimize multichannel transmit arrays, and it was free from most physiologic motion compared with other organs allowing quantitative B_1^+ mapping to be easily performed. Therefore, several general torso imaging arrays are presented as recently reviewed.[12]

A 16-channel micro-stripline array (16 ML) was developed in our laboratory[82] and used with a pTx system with 16 1 kW transmit channels[44] (Fig. 5A). Compared with an 8-channel version of the coil, the higher element count and density increased the transmit and

receive performance by 22% along with improved parallel imaging performance, providing sufficient transmit and SAR efficiency to perform many of the acquisitions required in a clinical prostate examination. However, increased element density came at the expense of complexity, and the usability of this array was somewhat limited due to its weight, rigid structure, and the necessity to manually tune and match the elements on each subject.

An 8-channel array composed of center-fed microstrip line resonators with meanders was presented by Orzada and colleagues.[73] This coil was lighter, as it used an air rather than a polytetra-fluoroethylene block as a dielectric and did not require patient-specific tuning and matching. Using this array, a multireader study looking at anatomic T2-weighted (T2w) image quality in patients reported “satisfactory” to “good” ratings for image quality and in the identification of anatomic structures. In 17 patients, pathologically confirmed prostate cancer was identified on pre-surgical T2w turbo spin echo (TSE) imaging in ~2 min in images acquired with $0.75 \times 0.75 \times 3$ mm^3 resolution.[83]

Dipole antenna arrays were introduced by Raaijmakers and colleagues[59] for prostate imaging. Subsequently, meanders were added to improve SAR efficiency by 50% without compromising B_1^+ efficiency. The average B_1^+ in prostates between 12 and 18 μT were obtained for volunteers imaged on pTx systems with 8 × 2 kW amplifiers[78] (Fig. 5B). In general, dipole antenna elements have favorable characteristics for body imaging such as improved B_1^+ efficiency at greater depths and more uniform transmit-receive profiles compared with striplines or loops[84] as shown in Fig. 5B. Practical advantages of the fractionated dipole array compared with the original stripline elements and similar to the meander striplines are the flexible housing, lighter weight, and the absence of subject-specific tuning and matching. By adding 16 receive-only elements to an 8-channel fractionated dipole transceiver array SNR gains of 1.7- to 2.8-fold were observed compared with the same individuals imaged on a 3 T with a local commercial receiver array.[76,85] Along with increased SNR, lesion contrast to noise also increased in the patients studied.

On the receive side, geometrically decoupled loops and dipoles have been shown to increase the SNR in the head[86,87] and later in the prostate.[85] For transmit, the benefits of the combination has been explored with a 16-channel combined loop-dipole transceiver array (16LD)[79] (Fig. 5C). Experimental results demonstrated that the 16LD had more than 20% higher SNR and B_1^+ transmit efficiency compared with both the previously detailed 16-channel stripline and a 10-channel version of the fractionated dipole array.[88] The 16LD is a preferable way of increasing channel count and element density as compared with the earlier 16-channel stripline array. The loops and dipoles of the 16LD are geometrically decoupled eliminating the need for active decoupling. In addition, the performance of the 16LD performed well at multiple locations and on subjects with various sizes without the need for subject-dependent tuning and matching just as with the micro-stripline with meanders[73] and the fractionated dipole.[78] Maintaining this characteristic as a plug-n-play coil is critical for clinical applications.

The benefits of combining resonance structures in a coil can be appreciated by understanding the unique and complimentary RF fields, both magnetic (B-fields) and electric (E-fields), they produce. The B-fields are used for imaging whereas the E-fields are

responsible for heating, which we of course try to minimize. Together with the tissue properties of density (ρ) and conductivity (σ), the *E*-fields are used to calculated SAR as given by the relation, $\mathrm{SAR}=\frac{1}{\mathrm{V}}\int_{\mathrm{sample}}\frac{\sigma|\mathrm{E}|^2}{\rho}\mathrm{dV}$. Fig. 6 shows an individual block of the 16LD coil (see Fig. 6A), which contains both a loop and a dipole resonance structure. The electric fields simulated for the dipole and loop elements of loop-dipole combination (see Fig. 6B).[79] The coupling between these 2 elements will be proportional to the dot-product of the *E*-fields associated with 2 elements, integrated over space, that is, $\left(\iiint\left(\vec{\mathrm{E}}_{\mathrm{L}}\cdot\vec{\mathrm{E}}_{\mathrm{D}}\right)\mathrm{dV}\right)$. Even though the electrical fields from the 2 elements are not orthogonal everywhere, there are regions where the dot product is the same in magnitude but opposite in sign, thus canceling their contributions to the integral. Manipulating the phase and magnitude of RF within and between blocks provides many options for managing the *B*-fields for improved imaging and *E*-fields to reduce SAR. In addition to prostate imaging, the 16LD array has been used in multiple applications throughout the torso (see Fig 6D).

Other arrays developed for imaging in the torso, or specifically optimized to image the heart, are shown in Fig. 7. Although some of the cardiac imaging evaluations have been successfully performed with relatively simple RF coils, imaging studies seeking increased parallel imaging performance, improved management of B_1^+, and increased SNR, and contrast homogeneity have used RF arrays with increasing numbers of channels.[56,70,74,77,81,89–92]

A modular 32-channel coil was designed using 8 independent building blocks conforming to the chest wall, with each block containing 4 transceiver loop elements (see Fig. 7A).[56] Simulation-based phase shimming optimizing homogeneity was applied, which increased transmit efficiency 30% compared with a standard CP-like mode. Along with supporting a 1D parallel imaging reduction factor of 4, cine imaging with 1.1 × 1.1 × 2.5 mm^3 was possible, which is 6-fold better than standard cine protocols at 1.5 T.

A 16-channel bow tie dipole antenna array arranged in 2 rows was shown to improve parallel imaging performance, contrast-to-noise ratio (CNR) and SNR compared with the 32-channel array (see Fig. 7B).[77] Although the form factor of this coil is bulky due to the D2O-filled containers used to shorten element lengths, it remains somewhat flexible to conform to the chest cavity. Benefitting from the favorable transmit profile of dipole elements demonstrated previously[78] B_1^+ uniformity improved in the heart, which is anteriorly positioned in the chest cavity. Further improvements in spatial resolution for cine imaging were reported with this array with acquisitions of 0.8 × 0.8 × 2.5 mm^3. These reported gains in resolution mirror the theoretic gains in sensitivity expected when progressing from 1.5 to 7 T.[18]

Although a direct comparison is difficult, several other body-oriented RF arrays endeavored to improve transmit and receive performance by including elements of different resonance structures. Two arrays that have loop-receiver arrays separate from the transmit elements are shown in Fig. 5C, D. First is a cardiac tailored version of the 8-channel fractionated dipole with a 16-channel loop receiver (see Fig. 7C).[81] By the addition of the 16 loops to the 8-channel dipole transceiver array, the SNR was increased 50%.[85] Second is the array presented by Rietsch and colleagues, which, similar to the previous coil, consists of 8 blocks

where each block is composed of a meander transceiver and 3 receive-only loop elements (ie, 8Tx/32Rx) (see Fig. 7D). Finally, Fig. 5E shows the previously described 16LD transceiver array, which has been used in an increasing number of cardiovascular applications[79] (see Fig. 5E).

Parallel Transmit Systems

Using pTx is mandatory to achieve acceptable UHF images in the human torso, as demonstrated by the rather inhomogeneous B_1^+ distribution illustrated in Figs. 3A and 4C. The RF transmit architecture to drive the transceiver arrays can be accomplished in different ways as recently reviewed.[12] The first human imaging demonstration of this technology was carried out in the human head at 7 T and used a single RF power amplifier, which fed into 8 ports or elements using a splitter or feeding network, providing static RF shimming capabilities (by adjusting the relative phase of each transmit channel) to improve field homogeneity.[38] To expand control over the different elements of the transceiver arrays, pTx architectures were conceived and implemented,[93] first on a 9.4 T head-only system[40] and later on the first 7 T whole body scanner.[3,39] The increased degrees of freedom afforded by the new pTx functionality was needed, as the RF shims required to satisfy the desired transmit profile depend on the RF coil, the object loading the coil, and the target of interest.[94] These initial systems used a single waveform generator from the spectrometer, but that waveform was modulated channel-wise by a programmable transmit phase and magnitude (gain) controller as inputs to channel-dependent RF power amplifiers. To supplement the standard power monitoring, additional home-grown channel-dependent monitoring hardware and software were implemented on which coil and target-specific time-averaged power limits could be set.[82,95] These initial pTx setups provided the needed flexibility to accomplish a wide range of static RF shimming applications in the body but were still mostly beneficial for smaller and/or targeted regions of interest as detailed later.

More recently, a new and more flexible version of pTx systems was developed and have been integrated into commercial UHF scanners where each transmit channel has its own synthesizer, thus permitting channel-dependent wave-forms.[94,96] This hardware further increases the degrees of freedom available for RF shimming. They allow dynamic RF shimming, which is differentiated from static RF shimming by the ability to modify channel-specific phase and magnitude during the RF pulse at a much smaller time scale. Such systems have permitted the development of a plethora of pTx RF pulses that deal with the transmit B1 inhomogeneity problem, and some of these more complex pulses have been used in UHF imaging of the human torso, such as multispoke pulses[45] and multiband multispoke pulses.[97] For such multichannel transmit systems, advanced power monitoring is typically implemented, allowing real-time channel specific complex recording of forward and reflected power, permitting the real-time prediction of local SAR through the use of virtual observation points (VOPs) assuming that appropriate EM simulations had been performed for the given coil and anatomy.[98,99]

Specific Absorption Rate and Safe Operation of Radiofrequency Coils

One of the most significant challenges facing ultra-high fields is SAR, that is, the power deposited into the subject. SAR increases with increasing magnetic fields due to the

correspondingly higher RF that must be used and becomes even more complex when efficiently using multichannel pTx technology to solve UHF B_1^+ problems.

Regulatory bodies, such as the Food and Drug Administration (FDA) in the United States, set limits for “global” and “local” SAR. Global SAR can be experimentally estimated, as all MR imaging scanners are equipped with hardware and software to do so. With a single-channel transmit coil, EM simulations of the specific coil loaded with different anatomic human models can be used to establish a correlation between global SAR and local SAR for that coil. This correlation, including a safety margin that accounts for possible variations among individuals, can then used to abide by global and local SAR limits based on the experimental measurement of total time-averaged power per kg of exposed tissue, giving an estimate of global SAR alone. This strategy may hold at magnetic field strengths less than or equal to 3 T when multichannel transmit coils with very few channels (eg, two) is used and where global SAR remains the primary limitation.

The afore-described approach, however, is not suitable for UHF applications of pTx. The greater problem at UHF is *local* SAR (ie, heating) resulting from the shorter wavelengths present at higher frequencies and the common use of local transmitters that are positioned closer to the body. The situation becomes even more complex, as the pTx systems used to manage RF field inhomogeneities also can create areas of higher local SAR even when reductions in total power are realized. Although a strategy similar to that used on lower field clinical scanners can still be used with UHF multichannel transmit systems (ie, monitoring global power to estimate local SAR), larger safety margins depending on the range of allowed pTx solutions are required. More commonly, peak local 10 g averaged SAR in one or more human body models are estimated using a validated RF coil model with a variety of shim settings,[44,77–80] and worst-case SAR levels from those shims are used to determine channel-specific power limits for human imaging. The resulting conservative power limits are only reasonable to use when deploying pTx with limited degrees of freedom (ie, phase-only RF shimming) or when highly conservative power limits can be used without negatively affecting the applications of interest. This approach has been extensively used, including in the very first 7 T head[19] and body[39,41,42] papers.[100–110]

Ideally, subject-specific local SAR estimates would be calculated in real time for each pTx solution in order to fully exploit pTx functionality. Currently, however, creating a subject-specific human body models and performing the needed EM simulations are time prohibitive within the time constraints of an MR imaging session. Approximations to this ideal are possible, however, as EM simulations with a particular RF coil can be performed beforehand from a family of body models and used to guide real-time SAR predictions on the scanner.[110] Precalculated simulations provide complex estimates of the EM fields generated by each transmit channel of the desired RF coil. By multiplying with a complex weighting function, which carries with it the amplitudes and phases of each transmit channel for a particular pTx implementation, SAR can be determined. To perform this calculation in real time on the scanner, VOPs are implemented to greatly reduce the calculation burden.[98] To address the impact of anatomic variations, several human body models can be used to generate VOPs for real-time SAR assessment or a fixed safety factor based on the known impact of anatomic variations can be used to scale the results. The use of VOP to enable real-time power

monitoring would allow the confident tailoring of power limits for each RF shim solution or pTx designed pulse run on the scanner. Doing so would avoid the limitation of assigning a fixed conservative estimate for power deposition for all scans. These methods and other strategies are slowly being validated and integrated on UHF systems and will be necessary to most effectively take advantage of pTx hardware while maintaining subject safety.[100–110]

A critical component to implementing a strategy to monitor and safely limit SAR is the process of RF coil validation. The goal of coil validation is to ensure that the model of the RF coil accurately represents physical implementation and to incorporate discrepancies between simulation and experimental results into safety factors when defining safe power deposition limits or when generating VOPs. This process is especially important given the growing numbers of home-built coils designed to maximize SNR and exploit the pTx capabilities of the MR imaging systems. The common approach adopted by different institutions is to validate EM models of the RF coil in phantoms via B_1^+ mapping, measurement of the scattering parameter matrix, and temperature measurements to assess local SAR.[63]

IMAGING THE HUMAN TORSO AT 10.5 T

Significant gains have been achieved for imaging the human body at 7 T as outlined earlier and in referenced papers; undoubtedly, however, such gains will continue to grow as the number of research sites focused on UHF work grow, and the installed base of the number of latest generation 7 T scanners increase. However, despite these successes at 7 T, the SNR and CNR of MR imaging measurements for many applications remain a limiting factor for the biomedical information content sought in such studies. This is certainly true in the brain where information on structural and functional connectivity, anatomy, and neuronal activity are pursued; in such applications, 7 T has enabled acquisition of images for function and connectivity in the millimeter to submillimeter space scale[1,4,111,112]; however, this is still a relatively course resolution in comparison to the spatial organization and architecture of the brain. The same can be said of the applications in the torso; 7 T has significantly improved the resolution limits, imaging times, and, in many cases, the available contrast for biomedical imaging with organ systems of the human torso. However, these gains are still not a match to the scope of biological problems faced in understanding organ function and dysfunction. Pushing against these limitations, we have numerous tools in our armamentarium, and one of these tools is clearly higher magnetic fields. As such, there are several efforts pursuing magnetic field strength significantly beyond 7 T[113] for imaging the brain as well as the organ systems of the human body and extremities. One of these efforts is work on whole-body human imaging at 10.5 T (447 MHz) in the CMRR. Although imaging human brain function and anatomy remains the primary motivation for the development of the 10.5 T system, the torso imaging is a target of interest and the first human studies performed at 10.5 T was of the human torso.[13]

Local transmitters close to the surface of the body have been the preferred approach for 7 T imaging in the human torso in the authors' laboratory, as detailed before. Following this approach, the authors started 10.5 T torso imaging effort with a 10-channel transceiver dipole array[20] and reported results obtained with simulations and experimental data using a

human-torso shaped phantom. This relatively simple RF array, where each element is heavily loaded by the body and far from its neighbors, was straightforward to validate and thus was approved for human imaging by the FDA before any RF coil designed for the head. Using this RF coil, human imaging was possible as an additional component to an ongoing 10.5 T safety study, allowing us to explore the feasibility and challenges of imaging the human torso at 447 MHz.

One of the primary questions in pursuing magnetic fields substantially higher than 7 T is whether one can deal with the expected transmit B_1 inhomogeneities and operate also within safe power deposition (ie, SAR) limits. This was evaluated through simulation for 10.5 T using the approved 10-channel transceiver dipole array in comparison to a similar antenna array configuration at 7.0 T.[20] Because of the higher Larmor frequency at 10.5 T, optimized dipole antenna element lengths were shorter than the similarly designed 7.0 T elements. Fig. 8 illustrates L-curves demonstrating the tradeoffs between excitation error (ie, Normalized Root Mean Square Error) and peak local SAR for various design scenarios using spoke pulses. Combining 2-spoke pulse design with our 10.5 T dipole array provided comparable (when imaging kidneys or heart) or even better (when imaging prostate) RF performance than single-spoke designs at 7 T. These data demonstrate that the issues of transmit B_1 inhomogeneities can be managed at 10.5 T using pTx, and operational conditions can be achieved where peak local SAR and the degree of B_1 inhomogeneities are comparable to what is currently obtained at 7 T.

In addition to exploring the role of pTx in the management of B_1^+ and local SAR at 10.5 T, EM simulations in the human torso-shaped phantom yielded relative SNR gains of greater than 2-fold compared with 7 T. Experimental measurements in the same phantom yielded SNR gains of 2.2-fold, demonstrating that the gains in SNR predicted by EM simulations can be realized in practice. The challenge will be to build and validate RF coils that allow us to manage B_1^+ and SAR while simultaneously realizing the promised gains in SNR compared with the highly optimized, state of the art receive only arrays at 3 T.

With the recent availability of the 10.5 T system for human imaging under an Investigational Device Exemption from the FDA, preliminary human images in the human torso were obtained using the aforementioned 10-channel dipole array. In these initial studies, static phase-only RF shimming optimized primarily for transmit efficiency provided sufficient B_1^+ peak performance and homogeneity to perform anatomic and quantitative imaging in the prostate. The small volume of the prostate enabled this relatively simple strategy to be successful. However, as the anatomic targets increased in size and asymmetry within the body, additional degrees of freedom were required either through phase and magnitude RF shimming (ie, one spoke pulses) or multispoke RF pulses to obtain the desired homogeneity in signal and contrast.

An example of these preliminary 10.5 T images in the pelvis is shown in Fig. 9. In these hip images, local phase-only shimming was used using ROIs that outlined the 2 femoral heads and associated cartilage in the coronal and axial planes with a negative ROI removing the bone, thus leaving the signal from a thin rim of soft tissue for optimization; this approach followed a protocol previously used for 7 T.[46] The restricted volume of the ROIs used for the

shimming naturally led to some image inhomogeneities in regions outside the ROI. Nevertheless, the acquired images demonstrate excellent lipid suppression throughout the pelvis, effective mitigation of B_1^+ inhomogeneity in the ROIs, and the ability to visualize fine structures on the 0.7-mm isotropic MEDIC images. Important tissue contrast was obtained through the acquisition of proton density (PD) weighted TSE images, allowing visualization of the labrum.

Fig. 10 displays examples of axial and coronal T2-weighted TSE images demonstrating the image quality of clinically relevant T2-weighted anatomic images of the prostate at 10.5 T. Again, only phase shimming was used within an ROI encompassing the prostate. By using efficiency or trade-off shimming solutions, average B_1^+ efficiency was approximately doubled, whereas inhomogeneity (measured by the coefficient of variation of the magnitude-of-sum of B_1^+ within the ROI) decreased more than factor of 2, suggesting the effectiveness of using phase shimming to mitigate B_1^+ inhomogeneity for this relatively small target.

Even images of the heart, a difficult target, were obtained at 10.5 T using multichannel transmit techniques established for 7 T, as shown in Fig. 11, which compares a 4-chamber cine acquisition acquired with simple phase shimming, with one using a single-spoke pTx pulse with channel-wise phase and magnitude optimization.

These first ever in vivo human imaging studies at 10.5 T demonstrated that previously developed RF management strategies for imaging at 7 T are effective in tackling the B_1^+ inhomogeneity at 10.5 T, allowing high-quality images to be acquired in multiple target anatomies throughout the human torso. It is evident, however, that further development of the RF coils and integration of pTx functionality is required. Target-specific RF pulses are needed to achieve more uniform transmit B_1 fields while optimizing for SAR efficiency because both peak B_1^+ and local SAR are limiting factors in many applications. In particular, significant new developments are expected in the RF coil arrays, incorporating many of the advanced features such as the loop-dipole combinations used at 7 T and increasing the number of transmit elements to more than 10, first to 16 that the instrument is currently capable of supporting and even going beyond to 32. The number of receive channels can also be increased independent of the number of transmit channels. The coil elements can be improved in transmit and receive performance using high permittivity materials with low conductivity, optimized in their properties for the frequency of interest; this approach would decrease the length of the dipoles used, allowing dense arrays to be constructed. All of these future developments will need careful design and evaluation efforts and ultimately accurate RF coil validation in order to realize these advances.

SUMMARY

Imaging of the human torso at high magnetic fields such as 4 T was considered almost an impossible task due to the short wavelength of the required RF relative to the object size, and this idea was cemented by the early, virtually unrecognizable images of the torso first reported at 4 T (see Fig. 4A). This skepticism was, in a way, a continuation of the doubts surrounding the use of high magnetic fields for imaging in the human body that existed since the early days of MR imaging. At that time, based on modeling the electrically lossy and

conductive human body tissue, it was suggested that sensitivity and RF penetration issues made imaging at frequencies beyond ~10 MHz (~0.24 T) inadvisable.[114] Especially after the launch of 7 T,[1] however, the UHF imaging community achieved critically important strides in our understanding of the physics of RF interactions in the human body, which in turn has led to solutions for the challenges posed by such UHF. As a result, the originally obtained poor image quality, as demonstrated in Fig. 4A obtained at 4 T, has progressed to the high-quality and high-resolution images obtained at 7 T and now at 10.5 T in the human torso. Despite these tremendous advances, work still remains to further improve the image quality and fully capitalize on the potential advantages UHF has to offer. Many potential improvements are well known to the practitioners in the field and simply need to be implemented. Inevitably, new technologies will be developed also, bringing new transformative changes and carrying UHF imaging of organ systems of the human torso to new heights.

Acknowledgments

DISCLOSURE

The work reported in this article coming from the Center for Magnetic Resonance Research (CMRR), University of Minnesota was supported by NIH grants NIBIB P41 EB015894, NIBIB P41 EB027061, and NIH S10 RR029672.

REFERENCES

1. Ugurbil K Imaging at ultrahigh magnetic fields: History, challenges, and solutions. Neuroimage 2018;168:7–32. [PubMed: 28698108]
2. Ugurbil K The road to functional imaging and ultra-high fields. Neuroimage 2012;62:726–35. [PubMed: 22333670]
3. Vaughan JT, Snyder C, DelaBarre L, et al. in Proc Intl Soc Mag Reson Med Vol. 16 213 (Seattle, Washington, 2006).
4. Ugurbil K Magnetic resonance imaging at ultra-high fields. IEEE Trans Biomed Eng 2014;61:1364–79. [PubMed: 24686229]
5. Umutlu L, Ladd ME, Forsting M, et al. 7 Tesla MR imaging: opportunities and challenges. Rofo 2014;186:121–9. [PubMed: 23996625]
6. Trattnig S, Bogner W, Gruber S, et al. Clinical applications at ultrahigh field (7T). Where does it make the difference? NMR Biomed 2016;29:1316–34. [PubMed: 25762432]
7. Kraft O, Quick HH. 7T: Physics, safety, and potential clinical applications. J Magn Reson Imaging 2017;46:1573–89. [PubMed: 28370675]
8. Niendorf T, Sodickson DK, Krombach GA, et al. Toward cardiovascular MRI at 7 T: clinical needs, technical solutions and research promises. Eur Radiol 2010;20:2806–16. [PubMed: 20676653]
9. Niendorf T, Paul K, Oezerdem C, et al. W(h)ither human cardiac and body magnetic resonance at ultrahigh fields? technical advances, practical considerations, applications, and clinical opportunities. Nmr Biomed 2016;29:1173–97. [PubMed: 25706103]
10. Stab D, Al Najjar A, O'Brien K, Strugnell W, Richer J, Rieger J, Niendorf T, Barth M. Cardiac Magnetic Resonance Imaging at 7 T. J Vis Exp 2019 10.3791/55853.
11. de Boer A, Hoogduin JM, Blankestijn PJ, et al. 7 T renal MRI: challenges and promises. MAGMA 2016;29:417–33. [PubMed: 27008461]
12. Erturk MA, Li X, Van de Moortele PF, et al. Evolution of UHF Body Imaging in the Human Torso at 7T: Technology, Applications, and Future Directions. Top Magn Reson Imaging 2019;28:101–24. [PubMed: 31188271]
13. He X, Erturk MA, Grant A, et al. First in-vivo human imaging at 10.5T: Imaging the body at 447 MHz. Magn Reson Med 2020;84:289–303. [PubMed: 31846121]

14. Ocali O, Atalar E. Ultimate intrinsic signal-to-noise ratio in MRI. Magn Reson Med 1998;39:462–73. [PubMed: 9498603]
15. Schnell W, Renz W, Vester M, et al. Ultimate signal-to-noise- ratio of surface and body antennas for magnetic resonance imaging. IEEE Trans Antennas Propag 2000;48:418–28.
16. Wiesinger F, Boesiger P, Pruessmann KP. Electrodynamics and ultimate SNR in parallel MR imaging. Magn Reson Med 2004;52:376–90. [PubMed: 15282821]
17. Guerin B, Villena JF, Polimeridis AG, et al. The ultimate signal-to-noise ratio in realistic body models. Magn Reson Med 2017;78:1969–80. [PubMed: 27917528]
18. Pohmann R, Speck O, Scheffler K. Signal-to-noise ratio and MR tissue parameters in human brain imaging at 3, 7, and 9.4 tesla using current receive coil arrays. Magn Reson Med 2016;75:801–9. [PubMed: 25820458]
19. Vaughan JT, Garwood M, Collins CM, et al. 7T vs. 4T: RF power, homogeneity, and signal-to-noise comparison in head images. Magn Reson Med 2001;46:24–30. [PubMed: 11443707]
20. Erturk MA, Wu XP, Eryaman Y, et al. Toward imaging the body at 10.5 tesla. Magn Reson Med 2017;77:434–43. [PubMed: 27770469]
21. Wiesinger F, Van de Moortele PF, Adriany G, et al. Parallel imaging performance as a function of field strength–an experimental investigation using electrodynamic scaling. Magn Reson Med 2004;52:953–64. [PubMed: 15508167]
22. Frischer JM, God S, Gruber A, et al. Susceptibility-weighted imaging at 7 T: Improved diagnosis of cerebral cavernous malformations and associated developmental venous anomalies. Neuroimage Clin 2012;1:116–20. [PubMed: 24179744]
23. Tkac I, Oz G, Adriany G, et al. In vivo 1H NMR spectroscopy of the human brain at high magnetic fields: metabolite quantification at 4T vs. 7T. Magn Reson Med 2009;62:868–79. [PubMed: 19591201]
24. Metzger GJ, Auerbach EJ, Warlick CA, et al. in Proc Intl Soc Mag Reson Med Vol. 20 4390 (Melbourne, Australia, 2012).
25. Liu G, Song X, Chan KW, et al. Nuts and bolts of chemical exchange saturation transfer MRI. NMR Biomed 2013;26:810–28. [PubMed: 23303716]
26. Li X, Bolan PJ, Ugurbil K, et al. Measuring renal tissue relaxation times at 7 T. NMR Biomed 2015;28:63–9. [PubMed: 25346367]
27. Metzger GJ, Auerbach EJ, Akgun C, et al. Dynamically applied B1+ shimming solutions for noncontrast enhanced renal angiography at 7.0 Tesla. Magn Reson Med 2013;69:114–26. [PubMed: 22442056]
28. Hess AT, Bissell MM, Ntusi NA, et al. Aortic 4D flow: quantification of signal-to-noise ratio as a function of field strength and contrast enhancement for 1.5T, 3T, and 7T. Magn Reson Med 2015;73:1864–71. [PubMed: 24934930]
29. Schmitter S, Schnell S, Ugurbil K, et al. Towards high-resolution 4D flow MRI in the human aorta using kt-GRAPPA and B1+ shimming at 7T. J Magn Reson Imaging 2016;44:486–99. [PubMed: 26841070]
30. Glover GH, Hayes CE, Pelc NJ, et al. Comparison of Linear and Circular-Polarization for Magnetic-Resonance Imaging. J Magn Reson 1985;64:255–70.
31. Bottomley PA, Andrew ER. RF magnetic field penetration, phase shift and power dissipation in biological tissue: implications for NMR imaging. Phys Med Biol 1978;23:630–43. [PubMed: 704667]
32. Barfuss H, Fischer H, Hentschel D, et al. Whole-body MR imaging and spectroscopy with a 4-T system. Radiology 1988;169:811–6. [PubMed: 3187004]
33. Barfuss H, Fischer H, Hentschel D, et al. In vivo magnetic resonance imaging and spectroscopy of humans with a 4 T whole-body magnet. NMR Biomed 1990;3:31–45. [PubMed: 2390452]
34. Yang QX, Wang J, Zhang X, et al. Analysis of wave behavior in lossy dielectric samples at high field. Magn Reson Med 2002;47:982–9. [PubMed: 11979578]
35. Van de Moortele PF, Akgun C, Adriany G, et al. (1) destructive interferences and spatial phase patterns at 7 T with a head transceiver array coil. Magn Reson Med 2005;54:1503–18. [PubMed: 16270333]

36. Ugurbil K, Garwood M, Ellermann J, et al. Imaging at high magnetic fields: initial experiences at 4 T. Magn Reson Q 1993;9:259–77. [PubMed: 8274375]
37. Lee JH, Garwood M, Menon R, et al. High contrast and fast three-dimensional magnetic resonance imaging at high fields. Magn Reson Med 1995;34:308–12. [PubMed: 7500867]
38. Adriany G, Van de Moortele PF, Wiesinger F, et al. Transmit and receive transmission line arrays for 7 Tesla parallel imaging. Magn Reson Med 2005;53:434–45. [PubMed: 15678527]
39. Vaughan JT, Snyder CJ, DelaBarre LJ, et al. Whole-body imaging at 7T: preliminary results. Magn Reson Med 2009;61:244–8. [PubMed: 19097214]
40. Vaughan T, DelaBarre L, Snyder C, et al. 9.4T human MRI: preliminary results. Magn Reson Med 2006;56:1274–82. [PubMed: 17075852]
41. Snyder CJ, DelaBarre L, Metzger GJ, et al. Initial results of cardiac imaging at 7 Tesla. Magn Reson Med 2009;61:517–24. [PubMed: 19097233]
42. Metzger GJ, Snyder C, Akgun C, et al. Local B1+ shimming for prostate imaging with transceiver arrays at 7T based on subject-dependent transmit phase measurements. Magn Reson Med 2008;59:396–409. [PubMed: 18228604]
43. Suttie JJ, Delabarre L, Pitcher A, et al. 7 Tesla (T) human cardiovascular magnetic resonance imaging using FLASH and SSFP to assess cardiac function: validation against 1.5 T and 3 T. NMR Biomed 2012;25:27–34. [PubMed: 21774009]
44. Snyder CJ, Delabarre L, Moeller S, et al. Comparison between eight- and sixteen-channel TEM transceive arrays for body imaging at 7 T. Magn Reson Med 2012;67:954–64. [PubMed: 22102483]
45. Schmitter S, Delabarre L, Wu X, et al. Cardiac imaging at 7 tesla: Single- and two-spoke radiofrequency pulse design with 16-channel parallel excitation. Magn Reson Med 2013;70:1210–9. [PubMed: 24038314]
46. Ellermann J, Goerke U, Morgan P, et al. Simultaneous bilateral hip joint imaging at 7 Tesla using fast transmit B(1) shimming methods and multichannel transmission - a feasibility study. NMR Biomed 2012;25:1202–8. [PubMed: 22311346]
47. Grams AE, Kraff O, Umutlu L, et al. MRI of the lumbar spine at 7 Tesla in healthy volunteers and a patient with congenital malformations. Skeletal Radiol 2011 10.1007/s00256-011-1197-0.
48. Orzada S, Maderwald S, Poser BA, et al. RF excitation using time interleaved acquisition of modes (TIAMO) to address B1 inhomogeneity in high-field MRI. Magn Reson Med 2010;64:327–33. [PubMed: 20574991]
49. Umutlu L, Kraff O, Orzada S, et al. Dynamic contrast-enhanced renal MRI at 7 tesla: preliminary results. Invest Radiol 2011;46:425–33. [PubMed: 21317791]
50. Umutlu L, Orzada S, Kinner S, et al. Renal imaging at 7 Tesla: preliminary results. Eur Radiol 2011;21:841–9. [PubMed: 20872006]
51. Frauenrath T, Hezel F, Heinrichs U, et al. Feasibility of cardiac gating free of interference with electromagnetic fields at 1.5 Tesla, 3.0 Tesla and 7.0 Tesla using an MR-stethoscope. Invest Radiol 2009;44:539–47. [PubMed: 19652614]
52. Frauenrath T, Hezel F, Renz W, et al. Acoustic cardiac triggering: a practical solution for synchronization and gating of cardiovascular magnetic resonance at 7 Tesla. J Cardiovasc Magn Reson 2010;12:67. [PubMed: 21080933]
53. von Knobelsdorff-Brenkenhoff F, Frauenrath T, Prothmann M, et al. Cardiac chamber quantification using magnetic resonance imaging at 7 Tesla-a pilot study. Eur Radiol 2010;20:2844–52. [PubMed: 20640427]
54. van Elderen SG, Versluis MJ, Webb AG, et al. Initial results on in vivo human coronary MR angiography at 7 T. Magn Reson Med 2009;62:1379–84. [PubMed: 19859918]
55. von Knobelsdorff-Brenkenhoff F, Tkachenko V, Winter L, et al. Assessment of the right ventricle with cardiovascular magnetic resonance at 7 Tesla. J Cardiovasc Magn Reson 2013;15:23. [PubMed: 23497030]
56. Graessl A, Renz W, Hezel F, et al. Modular 32-channel transceiver coil array for cardiac MRI at 7.0T. Magn Reson Med 2014;72:276–90. [PubMed: 23904404]

57. Niendorf T, Graessl A, Thalhammer C, et al. Progress and promises of human cardiac magnetic resonance at ultrahigh fields: a physics perspective. J Magn Reson 2013;229:208–22. [PubMed: 23290625]
58. Maas MC, Vos EK, Lagemaat MW, et al. Feasibility of T -weighted turbo spin echo imaging of the human prostate at 7 tesla. Magn Reson Med 2013 10.1002/mrm.24818.
59. Raaijmakers AJ, Ipek O, Klomp DW, et al. Design of a radiative surface coil array element at 7 T: the single-side adapted dipole antenna. Magn Reson Med 2011;66:1488–97. [PubMed: 21630342]
60. Wu X, Schmitter S, Auerbach EJ, et al. Simultaneous multislice multiband parallel radiofrequency excitation with independent slice-specific transmit B1 homogenization. Magn Reson Med 2013 10.1002/mrm.24828.
61. Schmitter S, Ugurbil K, Van de Moortele P-F. Multi-Band-Multi-Spoke pTX RF Pulse Design in the Heart at 7 Tesla: towards Faster, Uniform Contrast Cardiac CINE Imaging. Proc Int Soc Mag Reson Med 2014;22.
62. International Electrotechnical Commission (IEC). Particular requirements for the safety of magnetic resonance equipment for medical diagnosis. (2010) International Standard IEC 60601-2–33.
63. Hoffmann J, Henning A, Giapitzakis IA, et al. Safety testing and operational procedures for self-developed radiofrequency coils. NMR Biomed 2016;29:1131–44. [PubMed: 25851551]
64. Arteaga de Castro CS, Boer VO, Luttje MP, et al. Temporal B0 field variation effects on MRSI of the human prostate at 7 T and feasibility of correction using an internal field probe. NMR Biomed 2014;27:1353–60. [PubMed: 25212868]
65. Schmitter S, Wu X, Ugurbil K, et al. Design of parallel transmission radiofrequency pulses robust against respiration in cardiac MRI at 7 Tesla. Magn Reson Med 2015;74:1291–305. [PubMed: 25411131]
66. Metzger GJ, DelaBarre L, Bi X, et al. in Proc Intl Soc Mag Reson Med Vol. 19 116 (Montreal, Canada, 2011).
67. Vaughan JT, Adriany G, Snyder CJ, et al. Efficient high-frequency body coil for high-field MRI. Magn Reson Med 2004;52:851–9. [PubMed: 15389967]
68. Willinek WA, Gieseke J, Kukuk GM, et al. Dual Source Parallel Radiofrequency Excitation Body MR Imaging Compared with Standard MR Imaging at 3.0 T: Initial Clinical Experience. Radiology 2010;256:966–75. [PubMed: 20720078]
69. Snyder CJ, DelaBarre L, Tian J, et al. in Proc Intl Soc Mag Reson Med Vol. 18 3839 (Stockholm, Sweeden, 2010).
70. Snyder CJ, DelaBarre L, Metzger G, et al. in Proc Intl Soc Mag Reson Med Vol. 19 7375 (Montreal, Canada, 2011).
71. Orzada S, Bitz AK, Johst S, et al. Analysis of an Integrated 8-Channel Tx/Rx Body Array for Use as a Body Coil in 7-Tesla MRI. Front Physiol 2017;5:1–10.
72. Paska J, Cloos MA, Wiggins GC. A rigid, stand-off hybrid dipole, and birdcage coil array for 7 T body imaging. Magn Reson Med 2018;80:822–32. [PubMed: 29250833]
73. Orzada S, Quick HH, Ladd ME, et al. in Proc Intl Soc Mag Reson Med Vol. 17 3010 (Honolulu, HI, 2009).
74. Winter L, Kellman P, Renz W, et al. Comparison of three multichannel transmit/receive radiofrequency coil configurations for anatomic and functional cardiac MRI at 7.0T: implications for clinical imaging. Eur Radiol 2012;22:2211–20. [PubMed: 22653280]
75. Ipek O, Raaijmakers AJ, Lagendijk JJ, et al. Intersubject local SAR variation for 7T prostate MR imaging with an eight-channel single-side adapted dipole antenna array. Magn Reson Med 2014;71:1559–67. [PubMed: 23754584]
76. Rosenkrantz AB, Zhang B, Ben-Eliezer N, et al. T2-weighted prostate MRI at 7 Tesla using a simplified external transmit-receive coil array: correlation with radical prostatectomy findings in two prostate cancer patients. J Magn Reson Imaging 2015;41:226–32. [PubMed: 24259458]
77. Oezerdem C, Winter L, Graessl A, et al. 16-channel bow tie antenna transceiver array for cardiac MR at 7.0 tesla. Magn Reson Med 2016;75:2553–65. [PubMed: 26183320]
78. Raaijmakers AJ, Italiaander M, Voogt IJ, et al. The fractionated dipole antenna: A new antenna for body imaging at 7 Tesla. Magn Reson Med 2016;75:1366–74. [PubMed: 25939890]

79. Erturk MA, Raaijmakers AJ, Adriany G, et al. A 16-channel combined loop-dipole transceiver array for 7 Tesla body MRI. Magn Reson Med 2017;77:884–94. [PubMed: 26887533]
80. Rietsch SHG, Orzada S, Maderwald S, et al. 7T ultra-high field body MR imaging with an 8-channel transmit/32-channel receive radiofrequency coil array. Med Phys 2018;45:2978–90. [PubMed: 29679498]
81. Steensma BR, Voogt IJ, Leiner T, et al. An 8-channel Tx/Rx dipole array combined with 16 Rx loops for high-resolution functional cardiac imaging at 7 T. MAGMA 2018;31:7–18. [PubMed: 29177772]
82. Metzger GJ, van de Moortele PF, Akgun C, et al. Performance of external and internal coil configurations for prostate investigations at 7 T. Magn Reson Med 2010;64:1625–39. [PubMed: 20740657]
83. Vos EK, Lagemaat MW, Barentsz JO, et al. Image quality and cancer visibility of T2-weighted magnetic resonance imaging of the prostate at 7 Tesla. Eur Radiol 2014;24:1950–8. [PubMed: 24865699]
84. Raaijmakers AJ, Luijten PR, van den Berg CA. Dipole antennas for ultrahigh-field body imaging: a comparison with loop coils. NMR Biomed 2016;29:1122–30. [PubMed: 26278544]
85. Steensma BR, Luttje M, Voogt IJ, et al. Comparing signal-to-noise ratio for prostate imaging at 7T and 3T. J Magn Reson Imaging 2018 10.1002/jmri.26527.
86. Wiggins G, Zhang B, Cloos MA, et al. in Proc Intl Soc Mag Reson Med Vol. 21 2737 (Salt Lake City (UT), 2013).
87. Chen G, Laksshmanan K, Sodickson DK, et al. in Proc Intl Soc Mag Reson Med Vol. 23 3133 (Toronto, 2015).
88. Erturk MA, Raaijmakers AJE, Adriany G, et al. in Proc Intl Soc Mag Reson Med Vol. 23 3122 (Toronto, 2015).
89. Thalhammer C, Renz W, Winter L, et al. Two-dimensional sixteen channel transmit/receive coil array for cardiac MRI at 7.0 T: design, evaluation, and application. J Magn Reson Imaging 2012;36:847–57. [PubMed: 22706727]
90. Grassl A, Winter L, Thalhammer C, et al. Design, evaluation and application of an eight channel transmit/receive coil array for cardiac MRI at 7.0 T. Eur J Radiol 2013;82:752–9. [PubMed: 21920683]
91. Aussenhofer SA, Webb AG. An eight-channel transmit/receive array of TE01 mode high permittivity ceramic resonators for human imaging at 7T. J Magn Reson 2014;243:122–9. [PubMed: 24818565]
92. Bitz AK, Brote I, Orzada S, et al. in Proc Intl Soc Mag Reson Med Vol. 18 4720 (Stockholm, Sweeden, 2010).
93. Vaughan JT, Adriany G, Ugurbil K. Univeristy of Minnesota, assignee. Shim, gradient, and parallel imaging coil. (2003) U.S. patent 7,268,554 USA.
94. Hoult DI, Phil D. Sensitivity and power deposition in a high-field imaging experiment. J Magn Reson Imaging 2000;12:46–67. [PubMed: 10931564]
95. Bitz AK, Orzada S, Kraff O, et al. in Proc Intl Soc Mag Reson Med Vol. 17 4767 (Honolulu, HI, 2009).
96. Ibrahim TS, Lee R, Abduljalil AM, et al. Dielectric resonances and B(1) field inhomogeneity in UHFMRI: computational analysis and experimental findings. Magn Reson Imaging 2001;19:219–26. [PubMed: 11358660]
97. Schmitter S, Moeller S, Wu X, et al. Simultaneous multislice imaging in dynamic cardiac MRI at 7T using parallel transmission. Magn Reson Med 2017;77:1010–20. [PubMed: 26949107]
98. Eichfelder G, Gebhardt M. Local specific absorption rate control for parallel transmission by virtual observation points. Magn Reson Med 2011;66:1468–76. [PubMed: 21604294]
99. Alon L, Deniz CM, Carluccio G, et al. Effects of Anatomical Differences on Electromagnetic Fields, SAR, and Temperature Change. Concepts Magn Reson Part B Magn Reson Eng 2016;46:8–18. [PubMed: 27134586]
100. Katscher U, Voigt T, Findeklee C, et al. Determination of electric conductivity and local SAR via B1 mapping. IEEE Trans Med Imaging 2009;28:1365–74. [PubMed: 19369153]

101. Shrivastava D, Vaughan JT. A generic bioheat transfer thermal model for a perfused tissue. J Biomech Eng 2009;131:074506. [PubMed: 19640142]
102. Homann H, Bornert P, Eggers H, et al. Toward individualized SAR models and in vivo validation. Magn Reson Med 2011;66:1767–76. [PubMed: 21630346]
103. Voigt T, Homann H, Katscher U, et al. Patient-individual local SAR determination: in vivo measurements and numerical validation. Magn Reson Med 2012;68:1117–26. [PubMed: 22213053]
104. van Lier ALHMW, Raaijmakers A, Voigt T, et al. Electrical Properties Tomography in the Human Brain at 1.5, 3, and 7T: A Comparison Study. Magn Reson Med 2014;71:354–63. [PubMed: 23401276]
105. Alon L, Sodickson DK, Deniz CM. Heat equation inversion framework for average SAR calculation from magnetic resonance thermal imaging. Bioelectromagnetics 2016;37:493–503. [PubMed: 27490064]
106. Deniz CM, Alon L, Brown R, et al. Subject- and resource-specific monitoring and proactive management of parallel radiofrequency transmission. Magn Reson Med 2016;76:20–31. [PubMed: 26198052]
107. Murbach M, Neufeld E, Cabot E, et al. Virtual population-based assessment of the impact of 3 Tesla radiofrequency shimming and thermoregulation on safety and B1 + uniformity. Magn Reson Med 2016;76:986–97. [PubMed: 26400841]
108. Orzada S, Ladd ME, Bitz AK. A method to approximate maximum local SAR in multichannel transmit MR systems without transmit phase information. Magn Reson Med 2017;78:805–11. [PubMed: 27604749]
109. Eryaman Y, Lagore RL, Erturk MA, et al. Radiofrequency heating studies on anesthetized swine using fractionated dipole antennas at 10.5 T. Magn Reson Med 2018;79:479–88. [PubMed: 28370375]
110. Meliado EF, van den Berg CAT, Luijten PR, et al. Intersubject specific absorption rate variability analysis through construction of 23 realistic body models for prostate imaging at 7T. Magn Reson Med 2018 10.1002/mrm.27518.
111. De Martino F, Yacoub E, Kemper V, et al. The impact of ultra-high field MRI on cognitive and computational neuroimaging. Neuroimage 2018;168:366–82. [PubMed: 28396293]
112. Dumoulin SO, Fracasso A, van der Zwaag W, et al. Ultra-high field MRI: Advancing systems neuroscience towards mesoscopic human brain function. Neuroimage 2018;168:345–57. [PubMed: 28093360]
113. Nowogrodzki A The world's strongest MRI machines are pushing human imaging to new limits. Nature 2018;563:24–6. [PubMed: 30382222]
114. Hoult DI, Lauterbur PC. The sensitivity of the Zeugmatographic experiment involving human samples. J Magn Reson 1979;34:425–33.

KEY POINTS

- The ultrahigh magnetic field (UHF) imaging community achieved critically important strides in our understanding of the physics of radiofrequency (RF) interactions in the human body.
- Despite tremendous advances, work still remains to further improve the image quality and fully capitalize on the potential advantages UHF has to offer.
- Many potential improvements are well known to the practitioners in the field and simply need to be implemented. Inevitably, new technologies will also be developed , bringing new transformative changes and carrying UHF imaging of organ systems of the human torso to new heights.

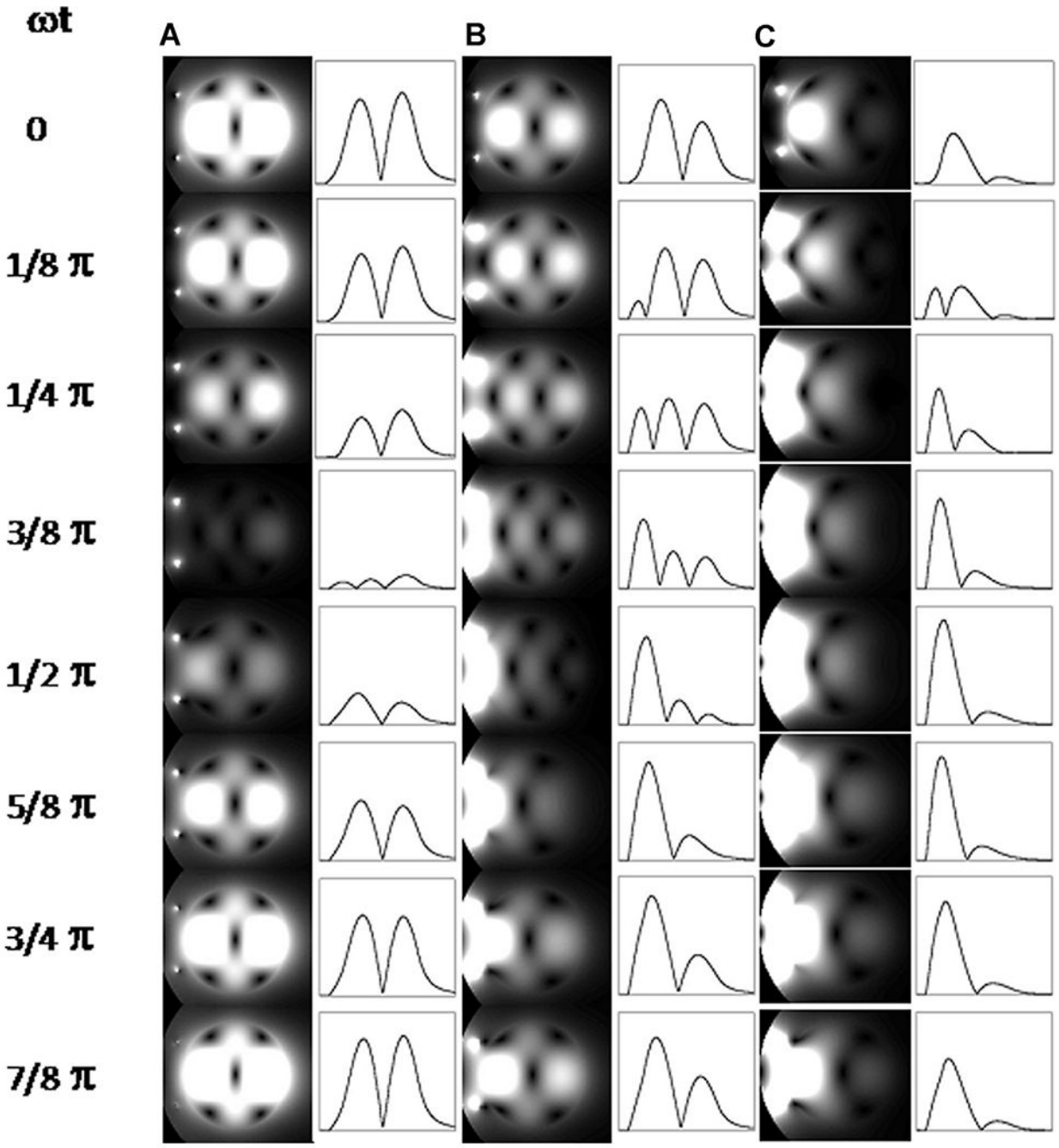

Fig. 1.

Two-dimensional (2D) plots of instantaneous transverse |B1| at progressing points during a half period in phantoms with (*A*) σ = 0 S/m, (*B*) σ = 0.26 S/m, and (*C*) σ = 0.67 S/m. The intensity profiles along the horizontal centerlines are also shown on the right of the 2D plots. The surface coil position is indicated by 2 small dots on the left side of the phantom. Because the temporal B1 strength varies greatly among these 3 cases, the signal intensities of temporal points are normalized individually for each conductivity condition in order to visualize the temporal change for all the conditions clearly.

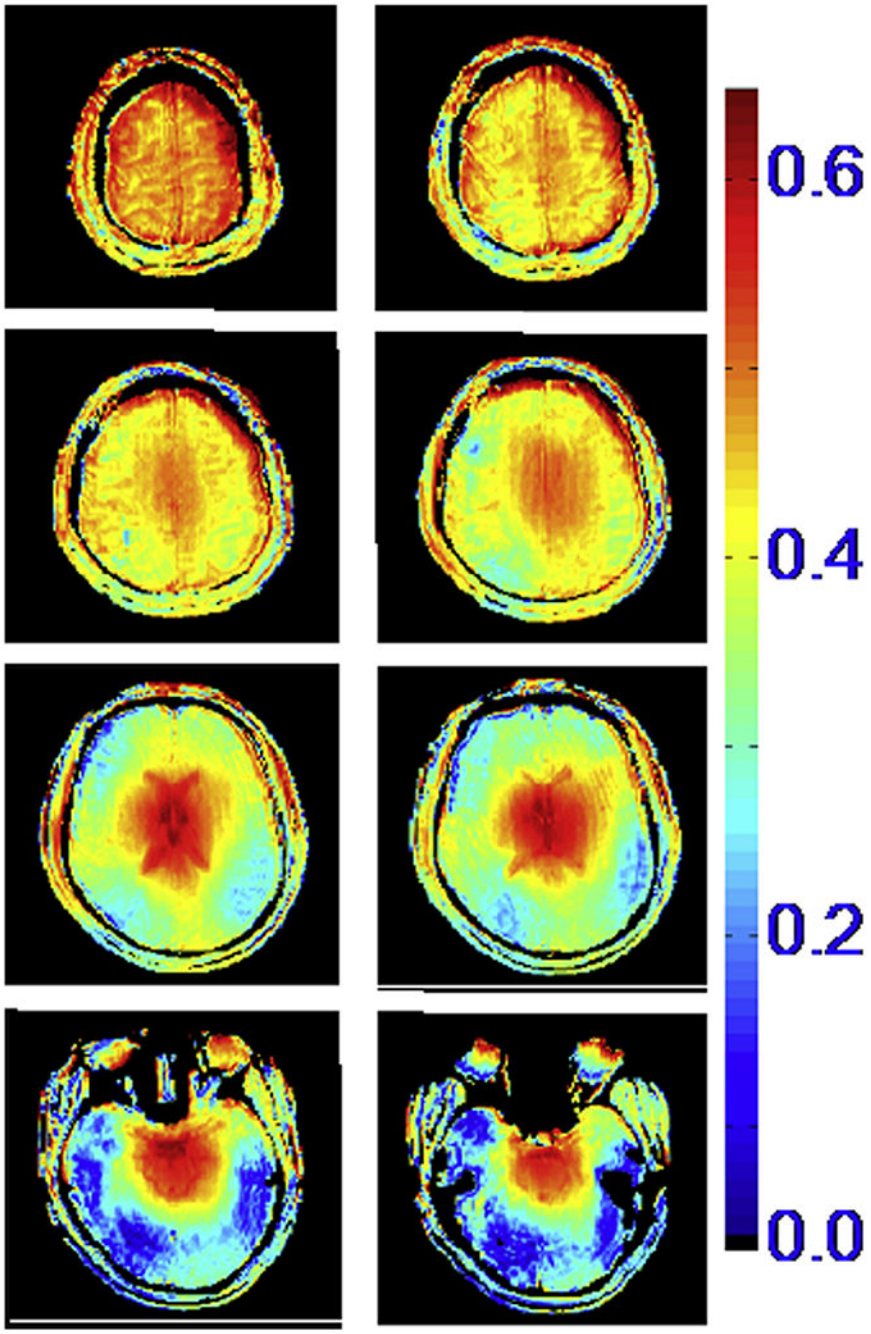

Fig. 2.

Transmit B1 magnitude in the human head at 7 T, generated by a volume TEM coil. The color code is proportional to μTesla/V.

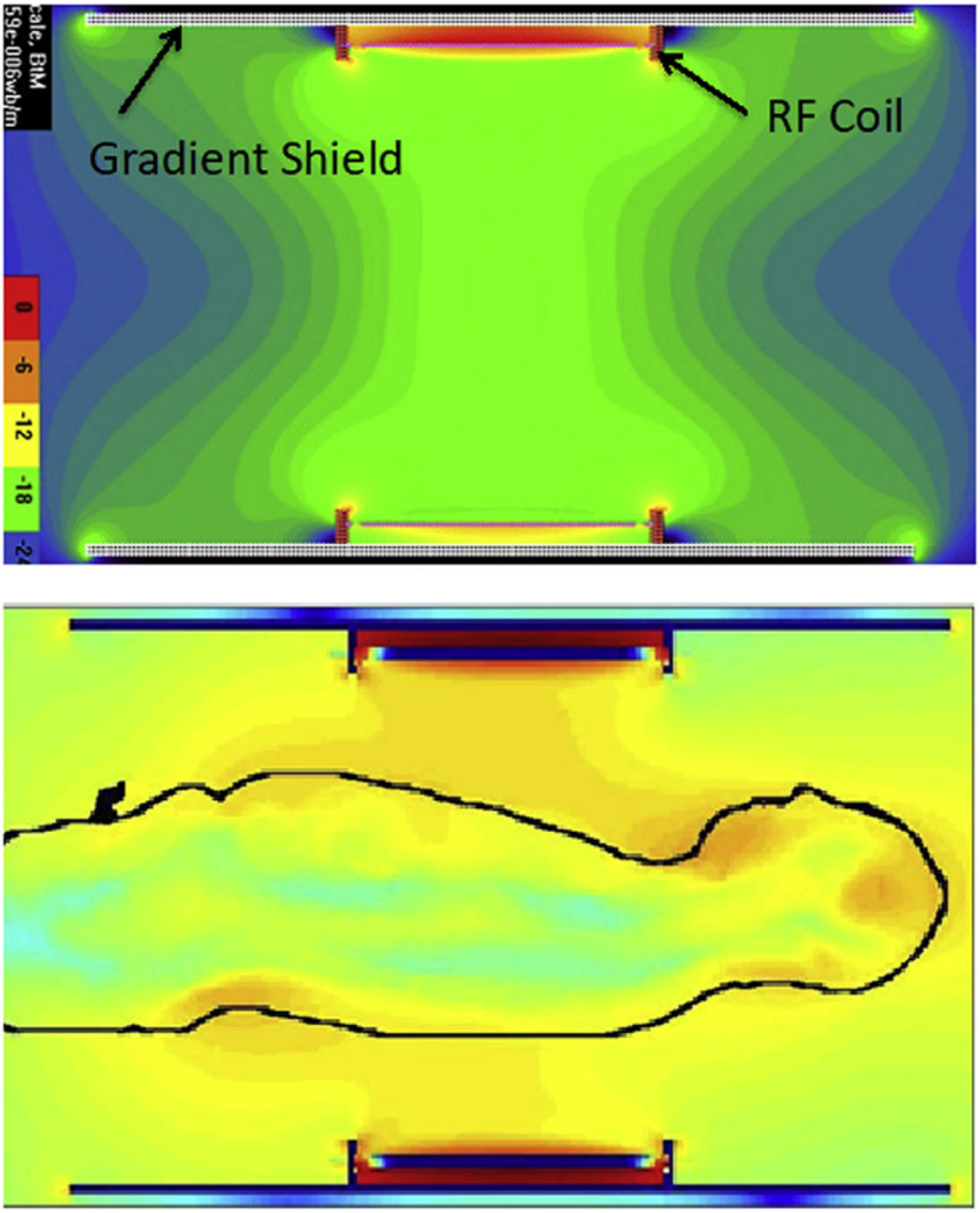

Fig. 3.

Electromagnetic simulations of the transmit B1 field in a body RF coil at 7 T. The coil produces a homogenous B1 when empty (*top figure*) but not when loaded with the human body (*lower figure*).

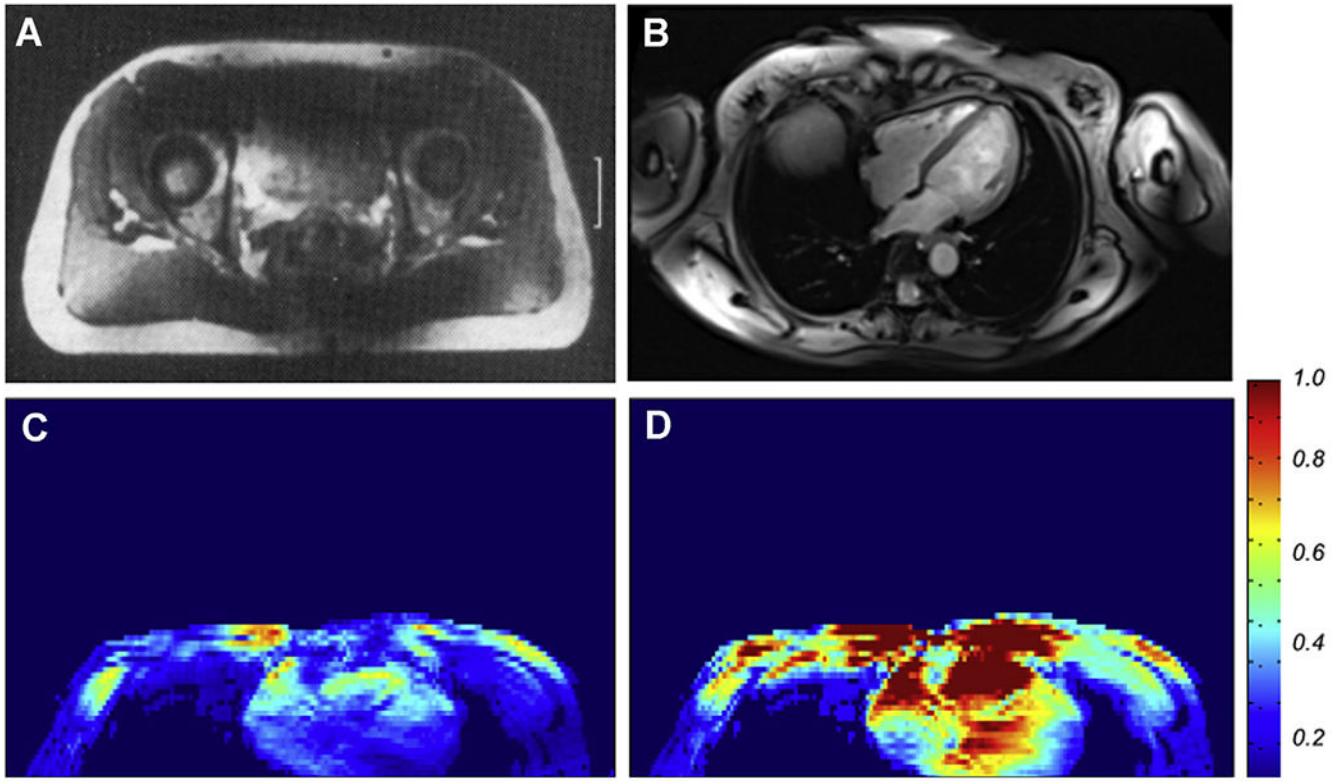

Fig. 4.

(*A*) Single axial slice image from the human pelvis reported from early 4 T experiments from the research laboratories of Siemens; (*B*), a contemporary 7 T image of an axial slice in the human torso, targeting imaging of the heart, obtained with a 16-channel transmit and receive array coil, using B1 "shimming". (*C*) and (*D*) The transmit B1 magnitude map before (*C*) and after (*D*) optimization over the heart in an axial slice approximately at the same position as that shown in Fig. 4B, demonstrating that the B1 is normally highly inhomogeneous and weak over this organ of interest (*C*) but can be improved significantly by multichannel transmit methods (*D*).

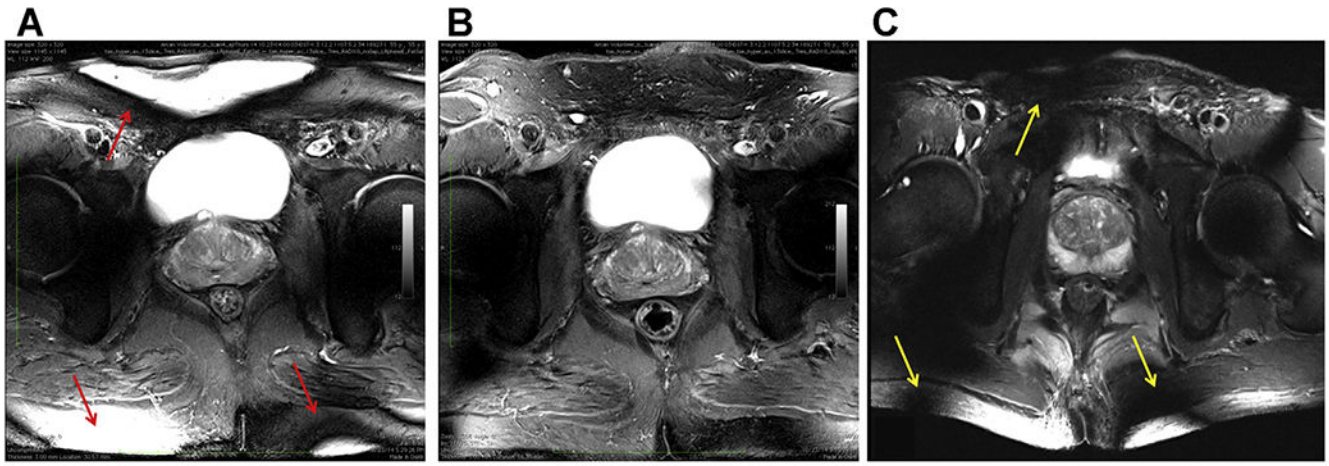

Fig. 5.

T2-weighted turbo spin echo anatomic images acquired with different body array configurations. (*A*) Image obtained with the original 16-channel micro-stripline (16 ML) with 8 anterior and 8 posterior elements and capacitive decoupling between adjacent ground planes and conductors. (*B*) Image obtained with a 10-channel fractionated dipole antenna (10DA) array with 6 anterior and 4 posterior elements. (*C*) Image obtained with the 16-channel loop-dipole array with 8 fractionated dipoles and centrally geometrically decoupled loops. All coils had similar circumferential coverage with their relative spacing to the nearest neighbor dictated by design. On quantitative analysis, the combination of loops and dipole elements (*C*) provided improved SNR and transmit efficiency. The uniform cross-sectional images produced by 10DA (*B*) highlight the benefits of the dipole resonant structure for body imaging in general. Although overflipping is more pronounced with the 16LD due to the inclusion of loop elements (*C*) on transmit (*yellow arrows*), the characteristically high B1+ gradient at the surface is more prevalent with the 16 ML (*red arrows*), again due to the presence of the surface coils. All data are from CMRR.

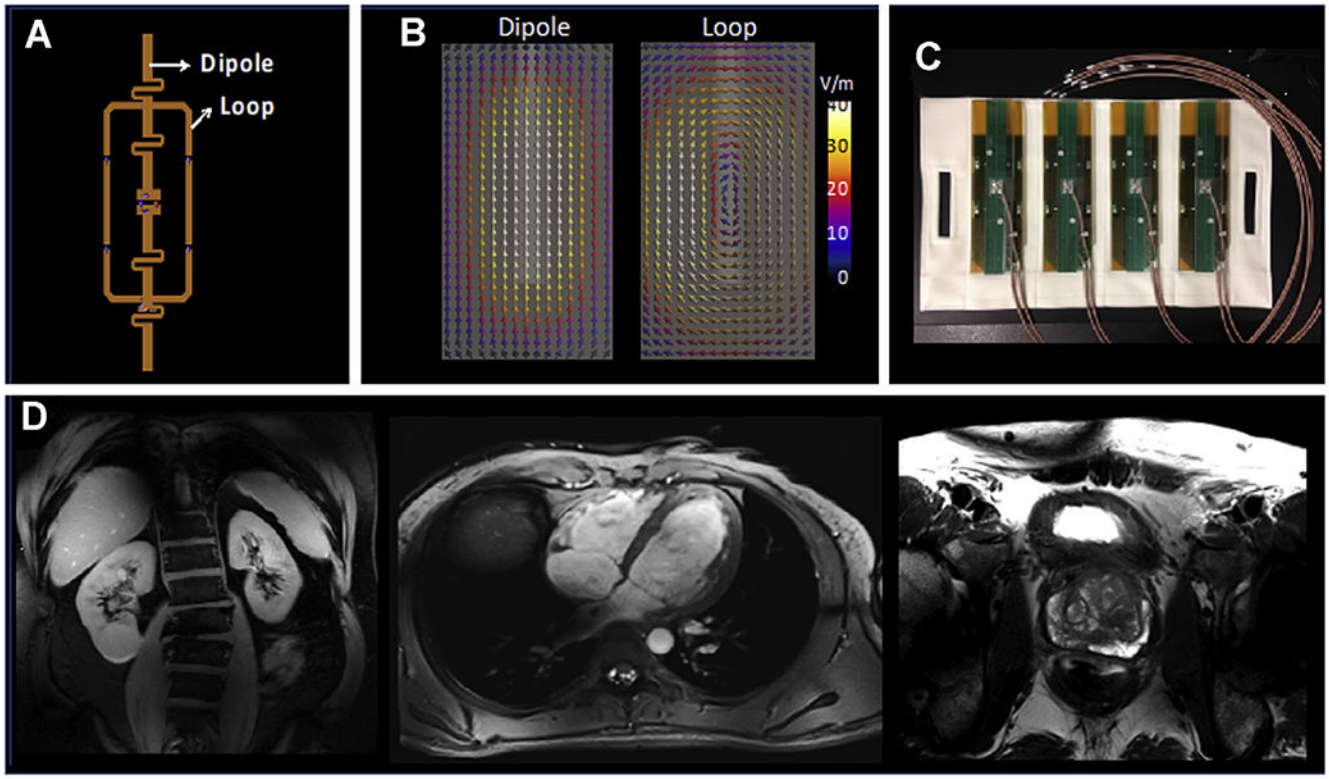

Fig. 6.

(*A*) The loop and dipole element within a single block of the 16LD coil used to generate the images in Fig.5C; (*B*) the electrical fields associated with the dipole and the loop elements, calculated by electromagnetic simulations. (*C*) Four loop-dipole blocks as manufactured containing the 8 transceiver channels for the anterior side of the 16LD coil. The same configuration is then placed also on the posterior side, as shown in Fig. 7E with a torso phantom. (*D*) Kidney, cardiac, and prostate images obtained with the 16LD coil.

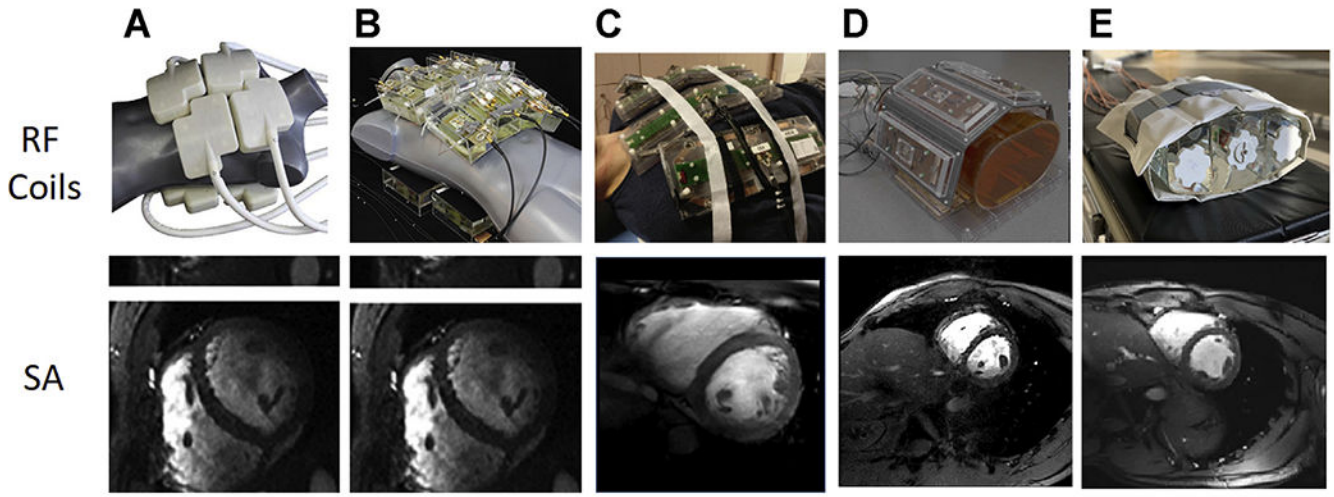

Fig. 7.

Single frames from short-axis (SA) cardiac cines acquired with 5 different 7 T body imaging arrays. (*A*) A 32-channel transceiver array consisting of 8 building blocks composed of 4 shielded loops in a 2 × 2 configuration per block. (*B*) An array composed of 16 building blocks each containing a bow tie-shaped λ/2-dipole antenna in a 4 × 2 configuration anterior and posterior. (*A*) and (*B*) used a universal RF shim solution based on EM simulations implemented through a splitter to produce a uniform field in the 4-chamber view. Images for (*A*) and (*B*) are acquired with resolutions of 1.1 × 1.1 × 2.5 mm3 and GRAPPA = 2 with acoustic cardiac triggering. (*C*) An 8 block array where each block is composed of a fractionated dipole transceiver and 2 receive only loops (ie, 8Tx/32Rx). The anterior elements are bent in the middle to better conform to the chest wall. Images were acquired with a resolution of 1.3 × 1.3 × 8 mm3 with subject-dependent phase-based RF shimming and VCG gating. (*D*) An 8-block array where each block is composed of a meander transceiver and 3 receive-only loop elements (ie, 8Tx/32Rx). RF shimming consisted of a universal phase-only RF shim and gating was performed with a finger pulse oximeter. Acquisition resolution was 1.5 × 1.5 × 3 mm3 with GRAPPA = 2 acceleration. (*E*) A 16-channel transceiver array with 4 loop-dipole blocks both anterior and posterior driven by a 16-channel pTx system using subject-specific static RF shim optimized for homogeneity over the heart. Acquisition parameters were 1 2 × 1.2 × 4 mm3 with GRAPPA = 2 and acquired with VCG gating. VCG, vectorcardiogram. (*Courtesy of*: Neindorf and Ozerdem (*A, B*); Steensma (*C*); Reitsch (*D*).)

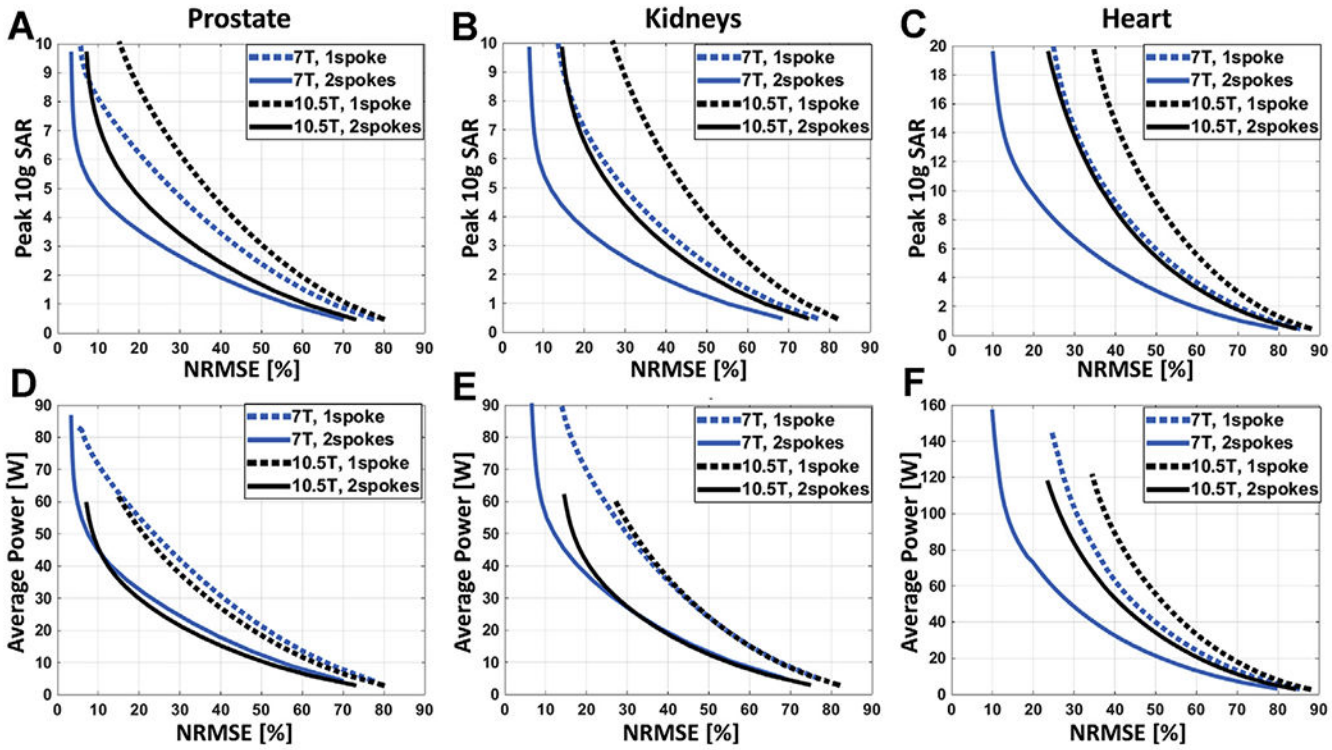

Fig. 8.

L-curves demonstrating the tradeoff between excitation error (Normalized Root Mean Square Error) and resulting peak local SAR for 7.0 T (blue) and 10.5 T (black) arrays when designing 1-spoke (dashed) and 2-spoke (solid) pTx pulses to image the prostate (*A*), the kidneys (*B*), and the heart (*C*). The pTx pulses were designed with explicit local SAR constraint, and the L-curve per design scenario was created by varying the predefined peak 10 g SAR limit. In all cases, the nominal flip angle was 45°.

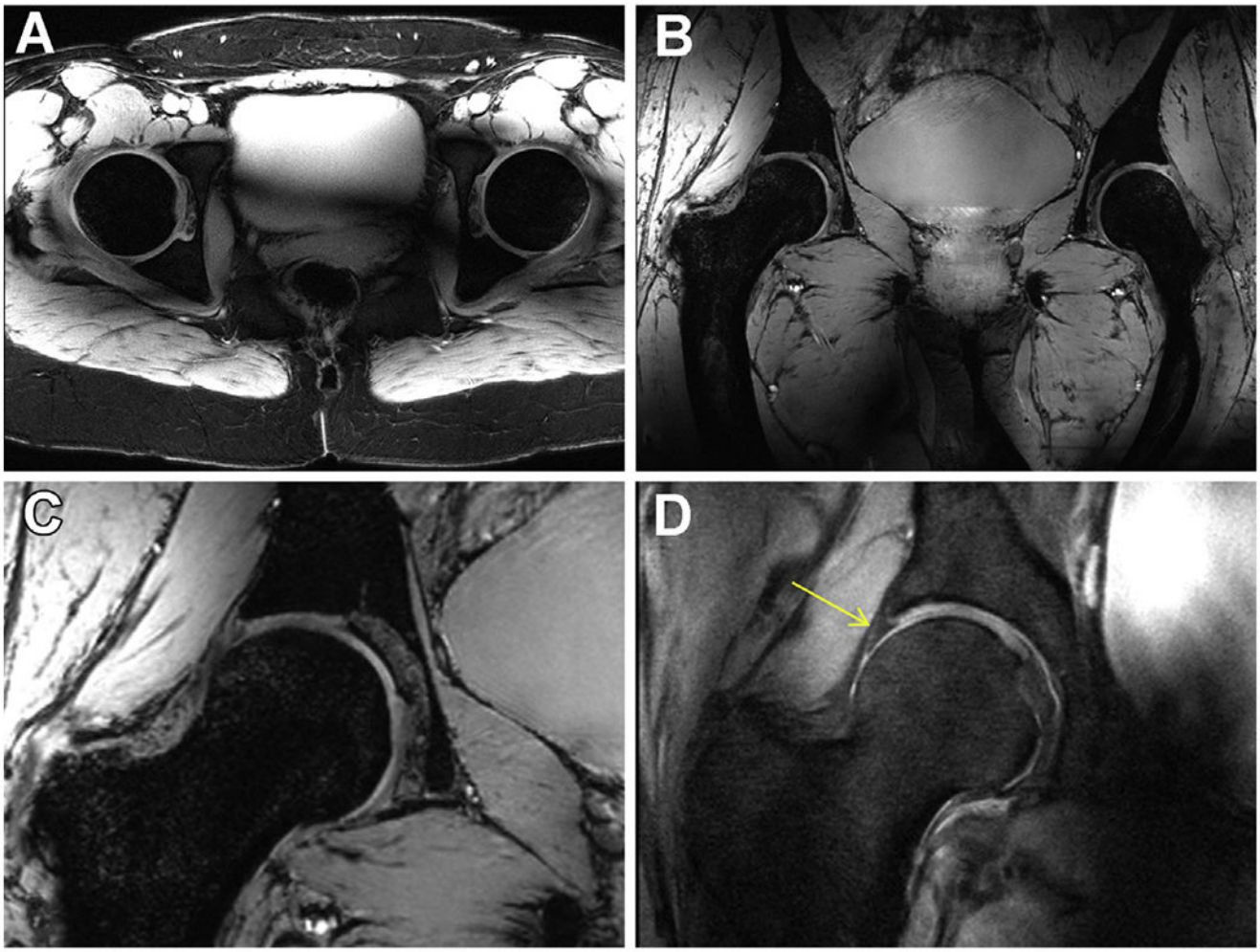

Fig. 9.

Anatomic hip imaging acquired at 10.5 T with a 10-channel dipole transceiver array. (*A*) An axial multislice 2D gradient echo acquisition acquired with fat saturation. (*B*) 3D coronal MEDIC acquisition. (*C*) Zoomed version of the right femoral head form the MEDIC (*B*) acquisition. (*D*) A proton-density (PD) weighted turbo spin echo (TSE) acquisition showing the expected contrast between the labrum and cartilage (*yellow arrow*).

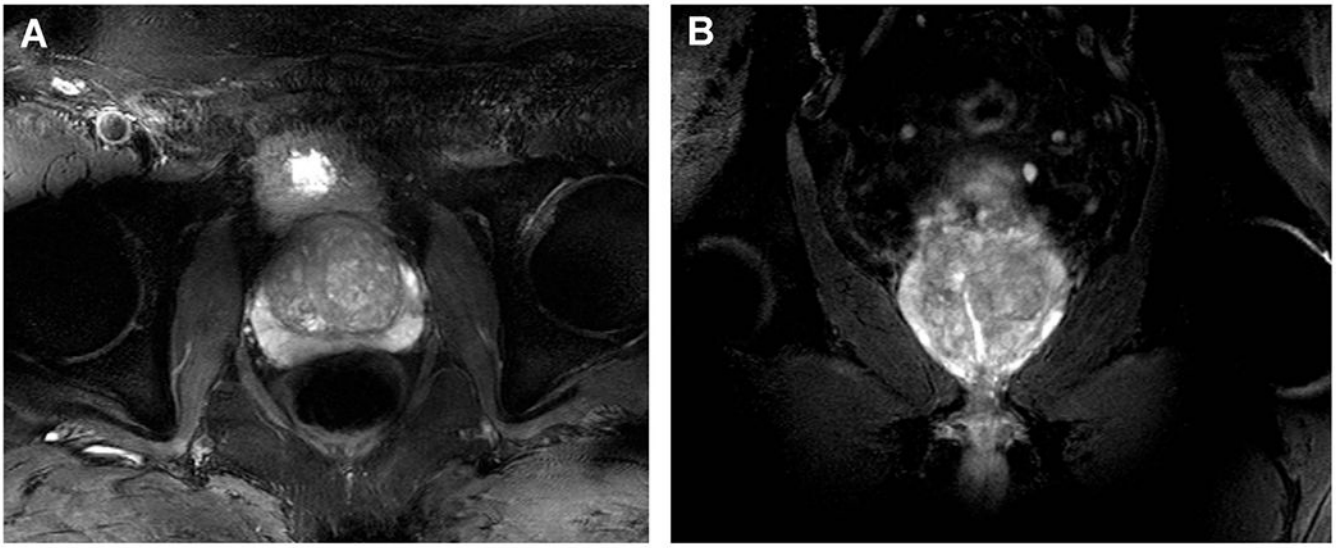

Fig. 10.

Initial images of the prostate at 10.5 T images. (*A*) Axial fat-suppressed T2w TSE, 9 slices, FOV 220 mm TR/TE: 7000/55 ms, resolution: 0.72 × 0.57 × 3mm3, TA: 05:30. (*B*) Coronal fat-suppressed T2w TSE, 9 slices, FOV 220 mm TR/TE: 7000/55 ms, resolution: 0.72 × 0.57 × 3mm3, TA: 05:30.

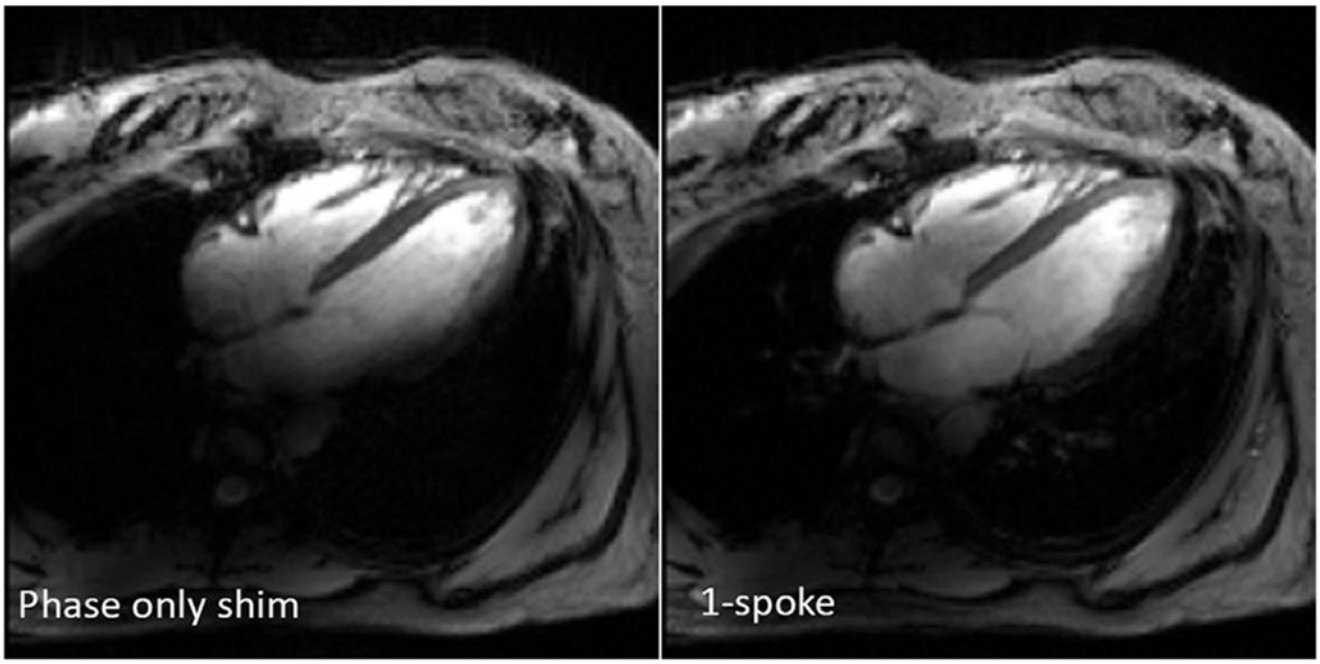

Fig. 11.

10.5 T cardiac images obtained with phase-only shim and 1-spoke pTx RF pulses, retrospectively gated GRE cine acquisition in the 4-chamber view.